Dynamic Inversion-Based Flare Control Law for Autonomous Helicopter Autorotation

Umberto Saetti *
Auburn University, Auburn, AL 36849, USA

Jonathan D. Rogers †
Georgia Institute of Technology, Atlanta, GA 30332, USA

Mushfiqul Alam ‡
Cranfield University, Cranfield, UK

Michael Jump § and Neil Cameron ¶
University of Liverpool, Liverpool, UK

A novel trajectory generation and control architecture for fully autonomous autorotative flare is proposed that combines rapid path generation with model-based control. The trajectory generation component uses optical Tau theory to compute flare trajectories for both longitudinal and vertical vertical speed. These flare trajectories are tracked by a nonlinear dynamic inversion (NDI) control law. One convenient feature of NDI is that it inverts the plant model in its feedback linearization loop, which eliminates the need for gain scheduling. However, the plant model used for feedback linearization still needs to be scheduled with the flight condition. This key aspect is leveraged to derive a control law that is scheduled with linearized models of the rotorcraft flight dynamics obtained in steady-state autorotation while relying on a single set of gains. Computer simulations are used to demonstrate that the NDI control law is able to successfully execute autorotative flare in the UH-60 aircraft. Autonomous flare trajectories are compared to piloted simulation data to assess similarities and discrepancies between piloted and automatic control approaches. Trade studies examine which combinations of downrange distances and altitudes at flare initiation result in successful autorotative landings.

I. Introduction

Autorotation is a complex maneuver that helicopter pilots must perform in the event of engine or transmission failure. The two main phases of autorotation consist of a steady-state descent phase, in which the aircraft uses inflow induced by vertical descent to maintain rotor speed within an acceptable range, and the flare, in which rotor kinetic energy is traded for reductions in the aircraft forward and vertical speeds. Recently, there has been increasing interest in automating helicopter autorotation maneuvers, or at least providing cues to pilots to enhance the probability of a successful outcome [1–8]. The steady-state descent phase of the maneuver is fairly straightforward to automate in the sense that the aircraft state can be driven to the known autorotative trim state using standard feedback control techniques. The challenge of automating the steady-state descent phase largely lies in planning a path to the selected landing point; this problem has been addressed in Ref. 6. Conversely, the flare maneuver is particularly difficult to automate due to the competing state constraints between forward, vertical, and rotor speeds, and also because the flare maneuver must be scaled and tailored according to the vehicle state condition as it nears the ground. For instance, if the aircraft initiates autorotation from a low speed and low altitude, the resulting flare maneuver will be short and will focus on rapidly arresting the vertical descent just before the vehicle touches down. In contrast, autorotations starting from high-energy flight conditions (higher altitude and/or higher speeds) require a more gradual flare initiated from a higher altitude.

Several authors have attempted to derive control laws for autorotation flare that adapt to the vehicle energy state as it nears the ground. This includes work by Tierney and Langelaan (Ref. 9), Sunberg *et al.* (Ref. 4), and Eberle and

*Assistant Professor, Department of Aerospace Engineering, Member AIAA.
†Lockheed Martin Associate Professor, Guggenheim School of Aerospace Engineering, Associate Fellow AIAA.
‡Lecturer, Cranfield University, Member AIAA.
§Senior Lecturer, University of Liverpool, Member AIAA.
¶Research Associate, University of Liverpool, Member AIAA

Rogers (Ref. 10). Despite the existing work in this area, there remains a need to develop flare control laws that can be computed online in real-time, and that use some type of model-based control to ensure that competing constraints on rotor and vehicle speeds are satisfied as much as possible. This work introduces a new trajectory generation and control architecture that combines rapid path generation with model-based control. The trajectory generation component of the architecture is similar to that proposed by Eberle and Rogers (Ref. 10). This trajectory generation scheme uses optical Tau theory to rapidly compute a solution to a two-point boundary value problem encompassing the initial vehicle state at flare initiation and the desired final vehicle state at touchdown. While in Ref. 10 this trajectory generator was envisioned primarily for pilot cueing, in the current work an automatic control loop is designed that tracks the desired trajectory to perform a fully-autonomous flare.

The flight control law used in this work to track the desired flare trajectory is nonlinear dynamic inversion (NDI), a popular model-following scheme among aircraft and rotorcraft manufacturers, and within the aerospace flight controls community in general. Application of NDI control laws to rotorcraft can be found in, *e.g.*, Refs. 11–15. A key aspect of DI is the reliance on model inversion to cancel the plant dynamics and track a desired reference model. One convenient feature of NDI is that it inverts the plant model in its feedback linearization loop, which, compared to other more conventional model-following control strategies such as explicit model following (EMF), eliminates the need for gain scheduling. However, the plant model used for feedback linearization still needs to be scheduled with the flight condition. NDI has also been applied to rotorcraft autorotation problems in a limited number of studies (Refs. 6, 16), but its use as a control law in autorotative flare has not been studied extensively to date.

As such, the objective of this study is to develop a trajectory planning and control algorithm for the autorotation flare that is capable of real-time implementation, adaptable to different entry conditions, and uses model-based control to satisfy competing state constraints. The two major contributions included in this paper are the following: (i) the extension of optical Tau theory for generating both longitudinal and vertical speed flare trajectories and (ii) the derivation of a NDI control law specifically meant for flare maneuvers that is scheduled with the linearized rotorocraft flight dynamics obtained in steady-state autorotation at varying speeds.

The paper begins with a description of the 6-degree-of-freedom helicopter simulation model used in control law development and simulation analysis. This is followed by detailed descriptions of the trajectory generation algorithm and DI control law. Simulation results demonstrate that the controller is able to successfully execute autorotative flare in the UH-60 aircraft. Autonomous flare trajectories are qualitatively compared to piloted simulation data to assess similarities and discrepancies between piloted and automatic control approaches. Trade studies examine the ability to extend or shorten the flare to reach a desired landing point.

II. Simulation Model

The helicopter flight dynamics model is a MATLAB® implementation of the helicopter model described in Ref. 17 and is representative of a utility helicopter similar to a UH-60. The model contains a 6-degree-of-freedom nonlinear rigid-body dynamic model of the fuselage, a quasi-static model of the blade flapping, and uses static aerodynamic models for fuselage, tail rotor inflows, and empennage. Main rotor inflow is modeled with a 1-state dynamic inflow model (Ref. 18). An additional degree of freedom is provided by the main rotor angular speed. The state vector is given by:

$$\boldsymbol{x}^T = [u\ v\ w\ p\ q\ r\ \phi\ \theta\ \psi\ x\ y\ z\ \lambda_0\ \Omega] \tag{1}$$

where:

u, v, w are the body-fixed velocities,
p, q, r are the angular rates,
ϕ, θ, ψ are the Euler angles,
x, y, z describe the position of the helicopter in the inertial frame,
λ_0 is the main rotor inflow, and
Ω is the main rotor angular speed.

The control vector is:

$$\boldsymbol{u}^T = [\theta_{1c}\ \theta_{1s}\ \theta_0\ \theta_{0T}] \tag{2}$$

where θ_{1c} and θ_{1s} are the lateral and longitudinal cyclic inputs, θ_0 is the collective input, and θ_{0T} is the tail rotor collective. It is worth noting that, because the helicopter model is only used in (unpowered) autorotation conditions in this study, no engine model and throttle inputs are included. A simple ground effect model is used to modify the thrust coefficient of the helicopter in proximity to the ground (Ref. 19).

III. Trajectory Generation

A key problem in the flare phase of autorotation is to generate trajectories that can be feasibly tracked by the helicopter while ensuring that the helicopter has minimal longitudinal and vertical speed at a desired downrange distance and at an altitude of a few feet over the ground. In the presented context, downrange distance is the longitudinal distance from the final touchdown longitdinal position. The approach that this paper will utilize is optical Tau theory (Ref. 20). In the context of helicopter flare maneuvers, it can be shown that longitudinal speed trajectories can be generated using the following equation (Refs. 10, 21):

$$V_x(t) = [V_x(0) - d_x] \left[1 - \frac{(k_{\text{opt}_1} - 1)\,[V_x(0) - d_x]\,t}{x(0)}\right]^{-1-\frac{1}{k_{\text{opt}_1}-1}} + d_x \tag{3}$$

where t is the time since the initiation of the flare, x is downrange distance, k_{opt_1} is a parameter that dictates the shape of the trajectory, and d_x is the final (small) longitudinal speed of the vehicle at touchdown. Given an initial downrange distance and longitudinal speed, and a total time to complete the deceleration, k_{opt_1} can be solved for in a deterministic manner by following the method in Ref. 10. It is worth noting that $k_{\text{opt}_1} \in [-1, 1]$. Previous approaches, such as the one in Ref. 10, used simple exponential trajectories for the vertical speed of the form:

$$V_z(t) = [V_z(0) - d_z]\, e^{-4t/\hat{T}} + d \tag{4}$$

where d_z is the final (small) vertical speed of the vehicle at touchdown. However, these exponential trajectories do not guarantee the helicopter to have a vertical speed d_z at a desired altitude $\hat{h}$ (typically a few feet over the ground). To compensate for this, the use of optical Tau theory is introduced also for the generation of vertical speed trajectories. This is a novelty compared to previous approaches in the literature. Similarly to longitudinal speed trajectories, vertical speed trajectories are generated using the following equation:

$$V_z(t) = [V_z(0) - d_z] \left[1 - \frac{(k_{\text{opt}_1} - 1)\,[V_z(0) - d_z]\,t}{h(0) - \hat{h}}\right]^{-1-\frac{1}{k_{\text{opt}_2}-1}} + d_z \tag{5}$$

where h is the altitude above the ground and $k_{\text{opt}_2} \in [-1, 1]$ is a parameter analogous to k_{opt_1}. These trajectories may then be fed to an outer-velocity loop for achieving a fully-autonomous flare maneuver. The computation of the total time of the maneuver, or time-to-contact with the ground, $\hat{T}$, can be performed following the heuristic approach proposed in Ref. 4. This approach is based on the vehicle's kinetic energy at the entry and exit of the flare maneuver.

Example longitudinal and vertical speed trajectories are derived for a UH-60 helicopter in autorotation at a total speed of 80 kts and weight of 16, 270 lb. These trajectories are shown in Fig. 1. Figure 1a shows longitudinal speed trajectories for varying downrange distances with desired final speed $d_x = 0$ and flare duration of $\hat{T} = 12$ seconds. Notably, for high downrange distances speed is decreased toward the end of the trajectory, whereas for low downrange distances speed is reduced more gradually. Similar observations can be made for vertical speed trajectories shown in Fig. 1b.

IV. Autonomous Flare Control Law

A multi-loop Dynamic Inversion (DI) control law largely based on Refs. 13, 16 is designed to enable fully autonomous flight of the helicopter in autorotation. The schematic of the closed-loop helicopter dynamics is shown in Fig. 2. The outer loop controller tracks longitudinal and lateral ground velocities commands in the heading frame and calculates the desired pitch and roll attitudes for the inner loop to track. The desired response type for the outer loop is Translational Rate Command (TRC). The inner loop achieves stability, disturbance rejection, and desired response characteristics about the roll, pitch, yaw, and heave axes. More specifically, an Attitude Command / Attitude Hold (ACAH) response is used for the roll and pitch axes, Rate Command / Attitude Hold (RCAH) is used for the yaw axis, and a TRC response is used for the heave axis. A generic DI controller as applied to a linear system is shown in Fig. 3. The key components are a command model (also known as command filter or reference model) that specifies desired response to pilot commands, a feedback compensation on the tracking error, and an inner feedback loop that achieves model inversion (*i.e.*, the feedback linearization loop).

A. Linear Models

The very first step toward the development of a DI flight control law is to obtain linear models representative of the rotorcraft flight dynamics across the flight conditions of interest. For this reason, linear models are derived by trimming

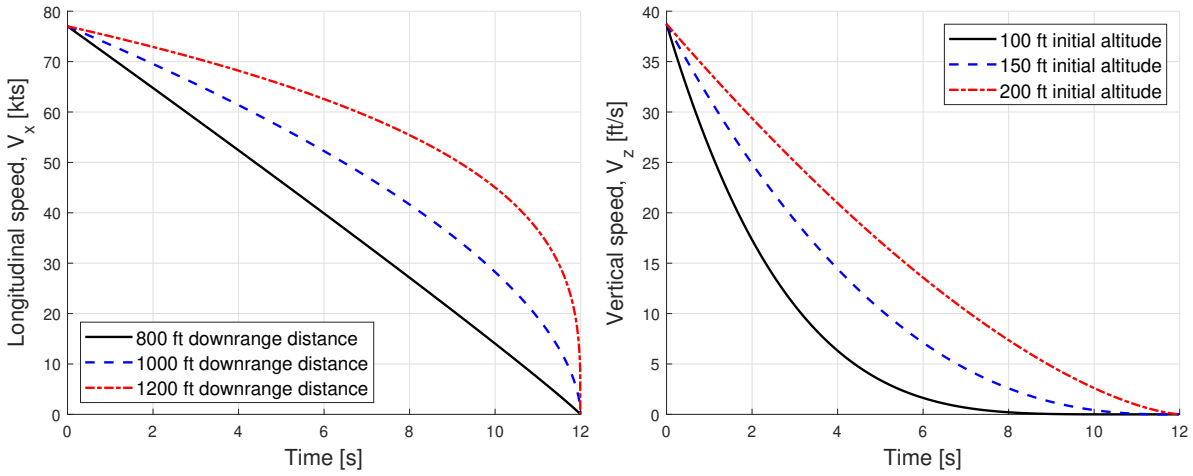

(a) Longitudinal speed.

(b) Vertical speed.

Fig. 1 Example longitudinal and vertical speed flare trajectories generated with optical Tau theory for varying downrange distances and initial altitudes.

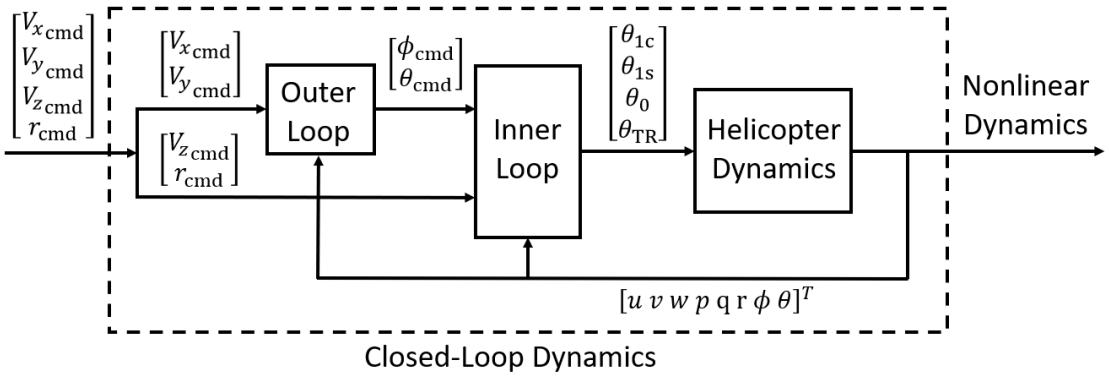

Fig. 2 Schematic of the closed-loop helicopter dynamics.

the rotorcraft at incremental longitudinal speeds V_x and subsequently linearizing about each trim condition:

$$\dot{\boldsymbol{x}} = \boldsymbol{A}(V_x)\boldsymbol{x} + \boldsymbol{B}(V_x)\boldsymbol{u} \tag{6}$$

where the coefficient matrices $\boldsymbol{A}$ and $\boldsymbol{B}$ are functions of the longitudinal speed of the aircraft. Because the control law is specifically meant for an autorotative maneuver, these linear models are obtained for an autorotation condition. That is, the trim variables are chosen as the following set of states and control inputs:

$$\boldsymbol{x}_{\text{trim}}^T = [u\ v\ w\ p\ q\ r\ \phi\ \theta\ \theta_{1c}\ \theta_{1s}\ \theta_0\ \theta_{0T}] \tag{7}$$

whereas the trim targets are:

$$\dot{\boldsymbol{x}}_{\text{des}}^T = \left[\dot{u}\ \dot{v}\ \dot{w}\ \dot{p}\ \dot{q}\ \dot{r}\ \dot{\phi}\ \dot{\theta}\ \dot{\psi}\ \dot{x}\ \dot{y}\ \dot{\Omega}\right] \tag{8}$$

All trim targets are set to zero except the derivative of the longitudinal position in the heading frame, which is set equal to the desired longitudinal speed (*i.e.*, $\dot{x} = V_x$). Note that the vertical speed in the heading frame, $\dot{z}$, is not included in the trim targets. This is because the vertical speed is defined by the longitudinal speed V_x and main rotor angular speed Ω that are assigned to the helicopter in autorotation. In autorotation, the main rotor angular speed is chosen as the nominal main rotor speed of the UH-60 (*i.e.*, $\Omega = 27$ rad/s) (Ref. 22). It is worth noting that, to the best knowledge of

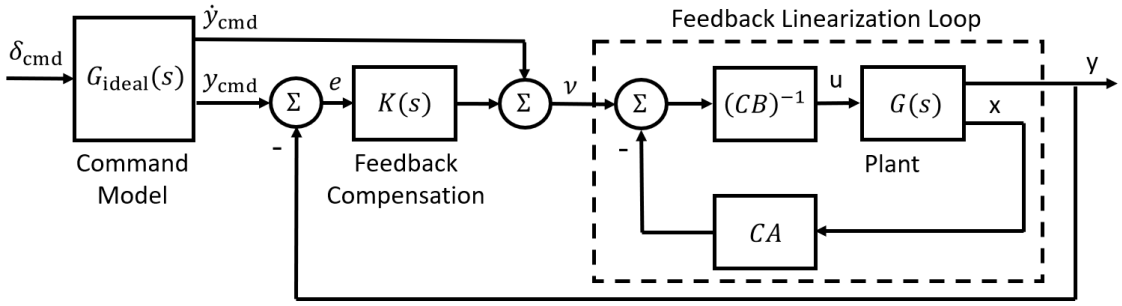

Fig. 3 DI controller as applied to a linear system.

the authors, the derivation of flight control laws for the flare portion of an autorotation maneuver based on linear models derived in a steady autorotation condition has not been examined previously.

An iterative algorithm based on Newton-Rhapson is used to trim the aircraft model at incremental speeds ranging from 0 to 100 kts at intervals of 20 kts. The aircraft weight chosen for this analysis is 17,000 lb. The results of this analysis are shown in Fig. 4. The trim attitude across this range of speeds is shown in Fig. 4a. Note that if the aircraft is trimmed with zero sideslip angle in powered level flight this would result in a non-zero bank angle. However, the trim bank angle in autorotation is zero because there is no torque exchanged between the main rotor and fuselage. Figure 4b shows the trim controls across the range of speeds in consideration. Notably, autorotation at low longitudinal speeds requires a high longitudinal cyclic control input. Finally, Fig. 4c shows the trim vertical speed with varying longitudinal speed. The vertical speed is shown to be minimum for a longitudinal speed equal to 60 kts. This minimum vertical speed is 37.5 ft/s, equivalent to about 2,250 ft/min.

B. Inner Loop

To model the inner-loop DI controller, a modified state vector is defined:

$$\hat{\boldsymbol{x}}^T = [u\ v\ w\ p\ q\ r\ \phi\ \theta] \tag{9}$$

along with modified system and control matrices $\hat{\boldsymbol{A}}(V_x)$ and $\hat{\boldsymbol{B}}(V_x)$. These modified matrices are found by truncating those rows and columns of matrices $\boldsymbol{A}(V_x)$ and $\boldsymbol{B}(V_x)$ corresponding to the states omitted in $\hat{\boldsymbol{x}}$. In addition, the following output vector is defined, corresponding to the controlled variables of the nonlinear system (*i.e.*, the aircraft dynamics):

$$\boldsymbol{y}^T = [\phi\ \theta\ r\ V_z] \tag{10}$$

where V_z is the vertical speed in the heading frame (positive up). The output matrix that relates the state vector to the output vector:

$$\boldsymbol{C} = \begin{bmatrix} \boldsymbol{C}_1 \\ \boldsymbol{C}_2 \end{bmatrix} \tag{11}$$

where:

$$\boldsymbol{C}_1 = \begin{bmatrix} 0 & 0 & 0 & 0 & 0 & 0 & 1 & 0 \\ 0 & 0 & 0 & 0 & 0 & 0 & 0 & 1 \end{bmatrix} \tag{12a}$$

$$\boldsymbol{C}_2 = \begin{bmatrix} 0 & 0 & 0 & 0 & 0 & 1 & 0 & 0 \\ 0 & 0 & -1 & 0 & 0 & 0 & 0 & V_x \end{bmatrix} \tag{12b}$$

$\boldsymbol{C}_1$ corresponds to the roll and pitch attitudes whereas $\boldsymbol{C}_2$ is related to the yaw rate and vertical speed. The matrix $\boldsymbol{C}_2$ is a function of the longitudinal speed V_x and therefore requires scheduling. This partitioning is due to the fact that the output equations for ϕ and θ must be differentiated twice to have the control inputs appear explicitly in the output

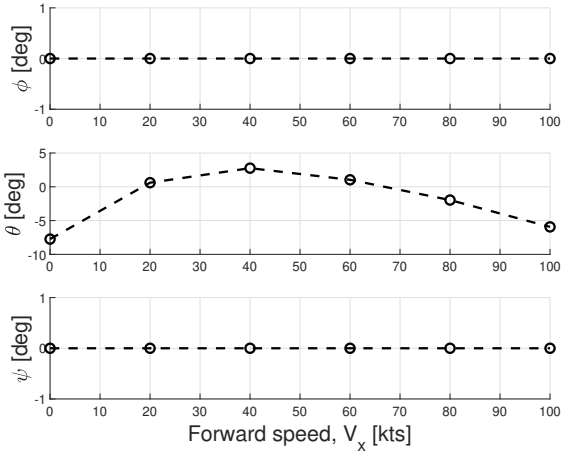

(a) Attitude.

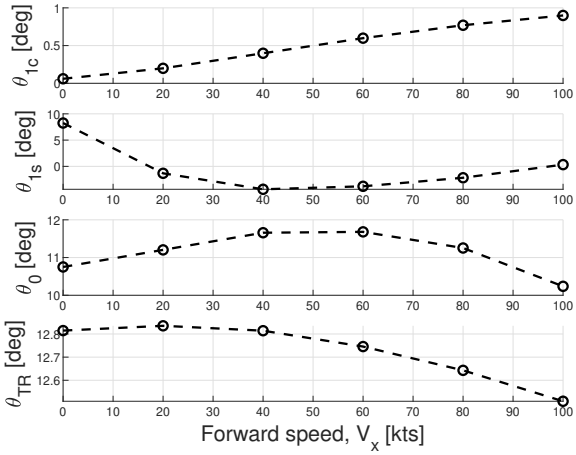

(b) Control inputs.

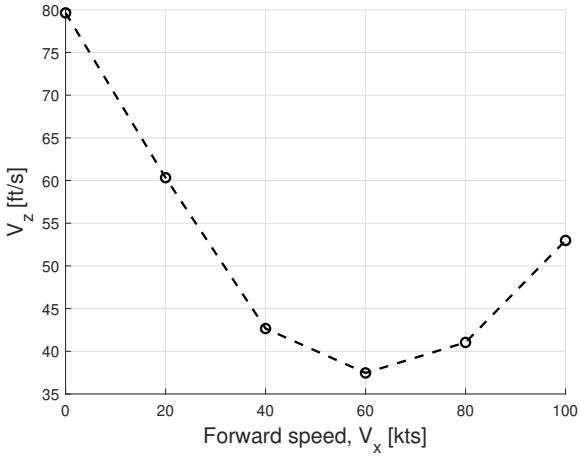

(c) Vertical speed.

Fig. 4 Trim variables with varying longitudinal speed.

equation, while the same procedure requires being performed once for r and V_z:

$$\begin{bmatrix} \ddot{\phi} \\ \ddot{\theta} \\ \dot{r} \\ \dot{V}_z \end{bmatrix} = \begin{bmatrix} \boldsymbol{C}_1 \hat{\boldsymbol{A}}^2 \hat{\boldsymbol{x}} + \boldsymbol{C}_1 \hat{\boldsymbol{A}} \hat{\boldsymbol{B}} \boldsymbol{u} \\ \boldsymbol{C}_2 \hat{\boldsymbol{A}} \hat{\boldsymbol{x}} + \boldsymbol{C}_2 \hat{\boldsymbol{B}} \boldsymbol{u} \end{bmatrix} \tag{13}$$

The objective of the DI control law is that the output $\boldsymbol{y}$ tracks a reference trajectory $\boldsymbol{y}_{\text{cmd}}(t)$ given by:

$$\boldsymbol{y}_{\text{cmd}}^T = \begin{bmatrix} \phi_{\text{cmd}} & \theta_{\text{cmd}} & r_{\text{cmd}} & V_{z\text{cmd}} \end{bmatrix} \tag{14}$$

with desired response characteristics. For this reason, the reference trajectory is fed through first- or second-order command models which dictate the desired response of the system. More specifically, ϕ_{cmd} and θ_{cmd} are fed through a second-order system, whereas r_{cmd} and $V_{z_{\text{cmd}}}$ are fed through a first-order system. The command models are also used to extract the first and second derivatives of the filtered reference trajectory for use in the proportional-integral (PI) and

Table 1 Inner loop command models parameters.

Command	ω_n [rad/s]	ζ
Roll Attitude, ϕ	4.5	0.7
Pitch Attitude, θ	4.5	0.7
Yaw Rate, r	2.0	-
Vertical Position, V_z	1.0	-

proportional-integral-derivative (PID) compensators described below. The command models are of the following form:

$$G^{(1)}_{\text{ideal}}(s) = \frac{1}{\tau s + 1} \tag{15a}$$

$$G^{(2)}_{\text{ideal}}(s) = \frac{\omega_n^2}{s^2 + 2\omega_n\zeta + \omega_n^2} \tag{15b}$$

where τ is the first-order command model time constant, which is the inverse of the command model break frequency (*i.e.*, $\tau = 1/\omega_n$). It is worth noting that this is not the optical Tau referred to earlier in the paper. Additionally, ω_n and ζ are, respectively, the natural frequency and damping ratio of the second-order command model. Table 1 shows the values used for the parameters of the command models of the inner loop.

PI and PID compensation are used to reject external disturbances and to compensate for discrepancies between the approximate model used in this derivation and the actual bare-airframe dynamics of the aircraft. The resulting DI control law is found by solving for the control vector in Eq. (13), leading to:

$$\boldsymbol{u} = \begin{bmatrix} \boldsymbol{C}_1\hat{\boldsymbol{A}}\hat{\boldsymbol{B}} \\ \boldsymbol{C}_2\hat{\boldsymbol{B}} \end{bmatrix}^{-1} \left(\boldsymbol{\nu} - \begin{bmatrix} \boldsymbol{C}_1\hat{\boldsymbol{A}}^2 \\ \boldsymbol{C}_2\hat{\boldsymbol{A}} \end{bmatrix} \hat{\boldsymbol{x}} \right) \tag{16}$$

where $\boldsymbol{\nu}$ is the pseudo-command vector and $\boldsymbol{e}$ is the error as defined respectively in Eqs. (17) and (18).

$$\begin{bmatrix} \nu_\phi \\ \nu_\theta \\ \nu_r \\ \nu_{V_z} \end{bmatrix} = \begin{bmatrix} \ddot{\phi}_{\text{cmd}} \\ \ddot{\theta}_{\text{cmd}} \\ \dot{r}_{\text{cmd}} \\ \dot{V}_{z_{\text{cmd}}} \end{bmatrix} + \boldsymbol{K}_P \begin{bmatrix} e_\phi \\ e_\theta \\ e_r \\ e_{V_z} \end{bmatrix} + \boldsymbol{K}_D \begin{bmatrix} \dot{e}_\phi \\ \dot{e}_\theta \\ 0 \\ 0 \end{bmatrix} + \boldsymbol{K}_I \begin{bmatrix} \int e_\phi dt \\ \int e_\theta dt \\ \int e_r dt \\ \int e_{V_z} dt \end{bmatrix} \tag{17}$$

$$\boldsymbol{e} = \boldsymbol{y}_{\text{cmd}} - \boldsymbol{y}; \tag{18}$$

The 4-by-4 diagonal matrices $\boldsymbol{K}_P$, $\boldsymbol{K}_I$, and $\boldsymbol{K}_D$ identify the proportional, integral, and derivative gain matrices, respectively. Note that the coefficient matrices $(\boldsymbol{C}_1\hat{\boldsymbol{A}}\hat{\boldsymbol{B}})^{-1}$, $\boldsymbol{C}_1\hat{\boldsymbol{A}}^2$, $(\boldsymbol{C}_2\hat{\boldsymbol{B}})^{-1}$, and $\boldsymbol{C}_2\hat{\boldsymbol{A}}$ are functions of the longitudinal speed of the aircraft V_x. For this reason, from a practical standpoint, these matrices are computed offline at incremental longitudinal speeds from 0 to 100 kts at 20 kts intervals and stored. When the linearized DI controller is implemented on the nonlinear aircraft dynamics, the coefficient matrices $(\boldsymbol{C}_1\hat{\boldsymbol{A}}\hat{\boldsymbol{B}})^{-1}$, $\boldsymbol{C}_1\hat{\boldsymbol{A}}^2$, $(\boldsymbol{C}_2\hat{\boldsymbol{B}})^{-1}$, and $\boldsymbol{C}_2\hat{\boldsymbol{A}}$ are computed at each time step via interpolation based on the current longitudinal airspeed $V_x(t)$ and on the lookup tables stored offline. It is important to note that what is implemented on the nonlinear aircraft dynamics is linearized DI. However, because the coefficient matrices are scheduled with the longitudinal speed, where scheduling effectively introduces a nonlinear relation between the aircraft states and the feedback control input, the controller implemented is effectively nonlinear DI (NDI) (Ref. 11). A block diagram of the linearized DI flight control law is shown in Fig. 5.

To ensure that the control inputs respect the maximum and minimum swashplate and tail rotor control inputs allowed by the UH-60 platform, the control inputs from the autonomous flare control law are saturated according to the specifications found in Ref. 22. The control inputs range are reported in Table 2.

C. Outer Loop

The objective of the outer loop is to track longitudinal and lateral velocities in the heading frame, such that the reference trajectory is given by:

$$\boldsymbol{y}^T_{\text{cmd}} = \begin{bmatrix} V_{x_{\text{cmd}}} & V_{y_{\text{cmd}}} \end{bmatrix} \tag{19}$$

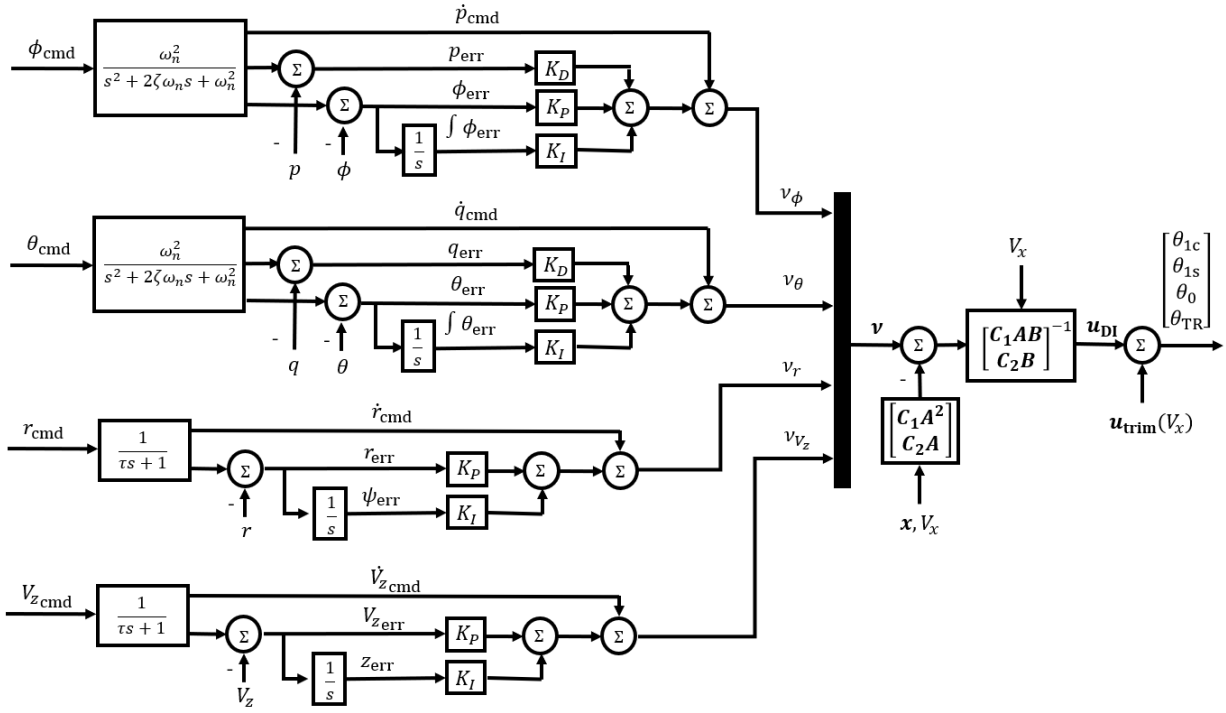

Fig. 5 Dynamic inversion inner loop.

Table 2 Swashplate and tail rotor control inputs range for UH-60 helicopter.

Control Input	Min. [deg]	Max. [deg]
Lateral Cyclic, θ_{1c}	-7	7
Longitudinal Cyclic, θ_{1s}	-12	12
Collective, θ_0	6.5	22.5
Tail Rotor Collective, θ_{0T}	-6	25

Table 3 Outer loop command models parameters.

Command	ω_n [rad/s]	ζ
Longitudinal Speed, V_x	1	0.7
Lateral Speed, V_y	1	0.7

The heading frame is a vehicle-carried frame where the x-axis is aligned with the current aircraft heading, the z-axis is positive up in the inertial frame, and the y-axis points to the right, forming a left-handed orthogonal coordinate system. The following equation shows the rotation from body to the heading frame:

$$\boldsymbol{T}_{h/b} = \begin{bmatrix} \cos\theta & \sin\phi\sin\theta & \cos\phi\sin\theta \\ 0 & \cos\phi & -\sin\phi \\ \sin\theta & -\sin\phi\cos\theta & -\cos\phi\cos\theta \end{bmatrix} \tag{20}$$

such that the velocities in the heading frame are given by:

$$\begin{bmatrix} V_x \\ V_y \\ V_z \end{bmatrix} = \boldsymbol{T}_{h/b} \begin{bmatrix} u \\ v \\ w \end{bmatrix} \tag{21}$$

The following approximate model of the longitudinal and lateral dynamics of the helicopter is used to derive the outer loop control law:

$$\underbrace{\begin{bmatrix} \dot{V}_x \\ \dot{V}_y \end{bmatrix}}_{\dot{\hat{\boldsymbol{x}}}} = \underbrace{\begin{bmatrix} X_u & 0 \\ 0 & Y_v \end{bmatrix}}_{\hat{\boldsymbol{A}}} \underbrace{\begin{bmatrix} V_x \\ V_y \end{bmatrix}}_{\hat{\boldsymbol{x}}} + \underbrace{\begin{bmatrix} -g & 0 \\ 0 & g \end{bmatrix}}_{\hat{\boldsymbol{B}}} \underbrace{\begin{bmatrix} \theta \\ \phi \end{bmatrix}}_{\boldsymbol{u}} \tag{22a}$$

$$\underbrace{\begin{bmatrix} x \\ y \end{bmatrix}}_{\boldsymbol{y}} = \underbrace{\begin{bmatrix} 0 & 1 & 0 & 0 \\ 0 & 0 & 0 & 1 \end{bmatrix}}_{\boldsymbol{C}} \underbrace{\begin{bmatrix} V_x \\ x \\ V_y \\ y \end{bmatrix}}_{\hat{\boldsymbol{x}}} \tag{22b}$$

where $\hat{\boldsymbol{x}}$ is the modified state vector, and $\hat{\boldsymbol{A}}(V_x)$, and $\hat{\boldsymbol{B}}$ are the modified system and control matrices. Note that these modified quantities are different from those used in the inner loop control design. The stability derivatives in the system matrix are scheduled with flight speed. The control matrix is not scheduled with speed as it is only composed of zeros and gravitational acceleration (*i.e.*, g). The output matrix $\boldsymbol{C}$ is also not scheduled with speed as it is composed solely of ones and zeros. The command models for the longitudinal and lateral speed are first order. The natural frequencies and damping ratios are given in Table 3. Following a similar procedure to the inner loop yields an outer control law of the form:

$$\boldsymbol{u} = \left(\boldsymbol{C}\hat{\boldsymbol{A}}\hat{\boldsymbol{B}}\right)^{-1}\left(\boldsymbol{\nu} - \boldsymbol{C}\hat{\boldsymbol{A}}^2\hat{\boldsymbol{x}}\right) \tag{23}$$

The reference trajectory is subtracted from the output to find the error, which is compensated by a PI controller. The feed-forward signal is subsequently added, leading to the pseudo-control vector for the outer loop:

$$\begin{bmatrix} \nu_x \\ \nu_y \end{bmatrix} = \begin{bmatrix} \dot{V}_{x_{\text{cmd}}} \\ \dot{V}_{y_{\text{cmd}}} \end{bmatrix} + \boldsymbol{K}_P \begin{bmatrix} e_x \\ e_y \end{bmatrix} + \boldsymbol{K}_I \begin{bmatrix} \int e_x dt \\ \int e_y dt \end{bmatrix} \tag{24}$$

The DI outer loop block diagram is shown in Fig. 6.

Because during flare the helicopter decelerates from relatively high-speed flight (i.e., greater than 60 kts) to low-speed flight (*i.e.*, lower than 40 kts), different control strategies are needed to control the yaw rate. Above 60 kts, turn

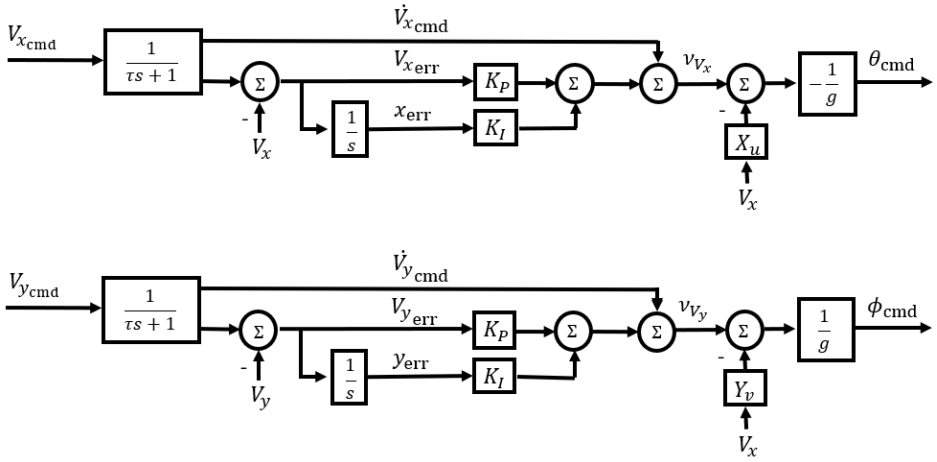

Fig. 6 Dynamic inversion outer loop.

coordination is used; below 40 kts no turn coordination (Ref. 23) is used; between 40 and 60 kts a blend between the two is used. These three control strategies are summarized as follows:

$$r'_{\text{cmd}} = \begin{cases} r_{\text{cmd}} & V < V_{\text{LS}} \\ r_{\text{cmd}} + \dfrac{g}{V}\sin\phi\left(\dfrac{V - V_{\text{LS}}}{V_{\text{HS}} - V_{\text{LS}}}\right) & V_{\text{LS}} \le V < V_{\text{HS}} \\ r_{\text{cmd}} + \dfrac{g}{V}\sin\phi & V \ge V_{\text{HS}} \end{cases} \tag{25}$$

where $V = \sqrt{V_x^2 + V_y^2 + V_z^2}$ is the total speed of the aircraft, $V_{\text{LS}} = 40$ kts, and $V_{\text{HS}} = 60$ kts.

To model the final pushover maneuver to level the rotorcraft before contact to the ground, the outer loop of the DI flight control law described above requires modifications. To induce a pushover prior to touchdown so that the helicopter lands with an acceptable pitch attitude, the pitch attitude command for tail wheel altitudes less than 6 ft is set to 0 deg. This pitch attitude command effectively bypasses the pitch attitude command from the outer-velocity loop when $h_{\text{TW}} \le 6$ ft. This ensures the helicopter pitches over before making contact with the ground, especially when descending at high pitch attitudes in the final stages of the flare maneuver. Thus the pitch attitude command to the inner loop is given by:

$$\theta'_{\text{cmd}} = \begin{cases} \theta_{\text{cmd}} & h_{\text{TW}} > 6\text{ft} \\ 0 \text{ deg} & h_{\text{TW}} \le 6\text{ft} \end{cases} \tag{26}$$

D. Error Dynamics

Feedback compensation is needed to ensure the system tracks the command models. It can be demonstrated (Ref. 24) that for a DI control law the output equation must be differentiated n times for the controls to appear explicitly in the output equation:

$$e^{(n)} = y_{\text{cmd}}^{(n)} - \nu \tag{27}$$

For those output equations that require to be differentiated only once, a PI control strategy is applied to the pseudo-command vector:

$$\nu = \dot{y}_{\text{cmd}}(t) + K_P e(t) + K_I \int_0^t e(\tau)d\tau \tag{28}$$

Substituting Eq. (28) into Eq. (27) leads to the closed-loop error dynamics:

$$\dot{e}(t) + K_P e(t) + K_I \int_0^t e(\tau)d\tau = 0 \tag{29}$$

The gains are chosen such that the frequencies of the error dynamics are of the same order as the command filters (*i.e.*, first order), ensuring that the bandwidth of the response to disturbances is comparable to that of an input given by a pilot or outer loop. By taking the Laplace transform, and therefore switching to the frequency domain, the error dynamics become:

$$e(s)\left(s^2 + sK_P + K_I\right) = 0 \tag{30}$$

To obtain the gains that guarantee the desired response, the error dynamics of Eq. (30) are set equal to the following second-order system:

$$s^2 + 2\zeta\omega_n s + {\omega_n}^2 = 0 \tag{31}$$

yielding the following proportional and integral gains:

$$K_P = 2\zeta\omega_n \tag{32a}$$

$$K_I = {\omega_n}^2 \tag{32b}$$

Similarly, for those outputs that require to be differentiated twice, a PID control strategy is applied to the pseudo-command vector:

$$\nu = \ddot{y}_{\text{cmd}}(t) + K_D\dot{e}(t) + K_P e(t) + K_I\int_0^t e(\tau)d\tau \tag{33}$$

Substituting Eq. (33) into Eq. (27) leads to the following closed-loop error dynamics:

$$\ddot{e}(t) + K_D\dot{e}(t) + K_P e(t) + K_I\int_0^t e(\tau)d\tau = 0 \tag{34}$$

and, therefore, to:

$$e(s)\left(s^3 + K_D s^2 + K_P s + K_I\right) = 0 \tag{35}$$

Again, the gains are chosen such that the frequencies of the error dynamics are of the same order as the command filters (*i.e.*, second order), ensuring that the bandwidth of the response to disturbances is comparable to that of an input given by a pilot or outer loop. To obtain the gains that guarantee the desired response, the error dynamics of Eq. (35) are set equal to the following third-order system:

$$(s^2 + 2\zeta\omega_n s + {\omega_n}^2)(s + p) = 0 \tag{36}$$

yielding the following proportional, integral, and derivative gains:

$$K_D = 2\zeta\omega_n + p \tag{37a}$$

$$K_P = 2\zeta\omega_n p + {\omega_n}^2 \tag{37b}$$

$$K_I = {\omega_n}^2 p \tag{37c}$$

This compensation strategy is used for ensuring trajectory tracking in both the inner and outer loops. Tables 4 and 5 show the natural frequencies, damping ratios, time constants, and the integrator pole values, respectively, for the inner and the outer loop. Note that the integrator pole p is usually chosen to be one-fifth of the natural frequency, corresponding to about one-fifth of the loop crossover frequency (Ref. 25). Further, the outer loop error dynamics natural frequency must be $1/10$ to $1/5$ of the inner loop error dynamics natural frequency to ensure sufficient frequency separation (Ref. 25). Additionally, because the plant is inverted in the feedback linearization loop such that the system being controlled is effectively a set of integrators, there is no need for gain scheduling. However, the plant model used for feedback linearization still must be scheduled with the flight condition (*i.e.*, with V_x in this case). Tables 6 and 7 show the compensation gains for the inner and outer loops.

V. Results

A. Demonstration of Autonomous Flare Control Law

To demonstrate the methodology, simulation results are compared to piloted flight simulations for the case of a flare maneuver initiated at 80 kts total speed, at a downrange distance of $1,000$ ft from the flare initiation point, for a flare

Table 4 Inner loop disturbance rejection natural frequencies, damping ratios, and integrator poles.

	ω_n [rad/s]	ζ	p
ϕ_{cmd}	4.5	0.7	0.75
θ_{cmd}	4.5	0.7	0.75
r_{cmd}	2	0.7	-
$V_{z_{\text{cmd}}}$	1	0.7	-

Table 5 Outer loop disturbance rejection natural frequencies and damping ratios.

	ω_n [rad/s]	ζ
$V_{x_{\text{cmd}}}$	1	0.7
$V_{y_{\text{cmd}}}$	1	0.7

Table 6 Inner loop compensation gains.

	K_P	K_I	K_D
ϕ_{cmd}	24.975	15.1875	7.05
θ_{cmd}	24.975	15.1875	7.05
r_{cmd}	4	4	4
$V_{z_{\text{cmd}}}$	2	1	-

Table 7 Outer loop compensation gains.

	K_P	K_I
$V_{x_{\text{cmd}}}$	1.5	0.5625
$V_{y_{\text{cmd}}}$	1.5	0.5625

initiation altitude of 140 ft. 80 kts was suggested in feedback to trials and presentations by UH-60 pilots. The gross weight of the UH-60 is set as 16, 270 lb. Piloted flight simulation results were obtained with the HELIFLIGHT-R flight simulator at University of Liverpool (Refs. 26, 27) and consist of 14 successful flare maneuvers conducted by a single former pilot. These piloted simulations are shown in Fig. 7, taken from Refs. 21, 28, 29. Each run is represented with different color. Figure 7a shows the longitudinal and vertical speed at which the flare maneuvers are initiated. Notably, initial vertical speeds vary approximately between −40 and −25 ft/s, whereas initial longitudinal speeds are mostly close to 80 kts. This is because the pilot was instructed to perform autorotations at 80 kts. Figure 7b shows longitudinal position and altitude trajectories. Downrange distances at which flare is initiated vary from approximately 850 to 1,150 ft, whereas initial altitudes span 120 to 190 ft. Figure 7c shows rotor speed, collective pitch input, and pitch attitude time histories. This figure suggests a trend in which pushover is initiated at about 3 to 5 seconds prior to touchdown.

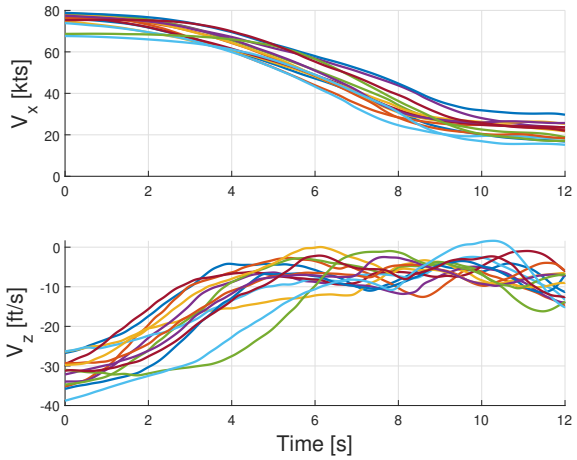

(a) Heading frame velocities.

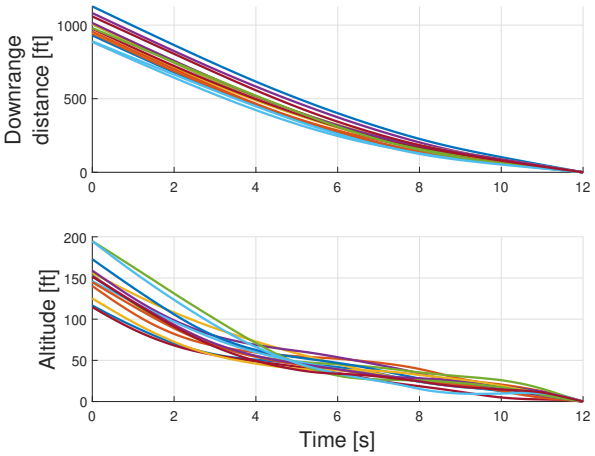

(b) Position.

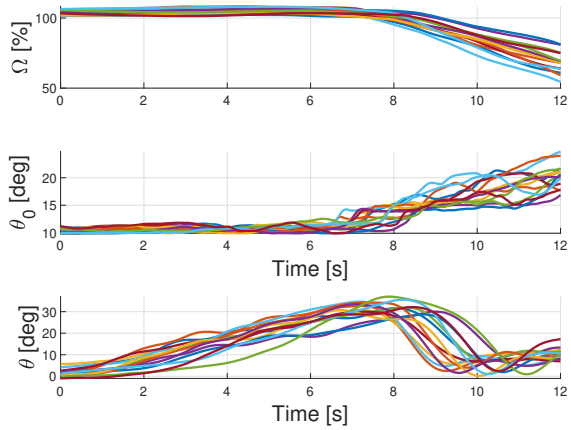

(c) Rotor speed, collective pitch input, and pitch attitude.

Fig. 7 Flare trajectories from piloted flight simulations.

The duration of the flare maneuver used in trajectory generation is chosen as the average time elapsed between the initiation of flare and touchdown as observed in the piloted simulations, *i.e.*, 12 seconds. To compare pilot flare strategy with that from the proposed method, parameters of the piloted simulations are averaged at each time step over the 12 seconds preceding touchdown. Comparison results are shown in Fig. 8. Figure 8a shows the longitudinal and vertical velocity trajectories generated with Tau theory (dashed red line). These trajectories result in the optimal parameters $k_{\text{opt}_1} = 0.3387$ and $k_{\text{opt}_2} = 0.7315$. This figure also shows excellent tracking by the closed-loop helicopter model of the

trajectories generated with Tau theory up until the pushover. When pushover is initiated, because of the proximity of the helicopter tail wheel to the ground, longitudinal velocity tracking is effectively no longer enforced as pitch angle is commanded directly to the controller inner loop. This causes the longitudinal speed to remain approximately constant after the initiation of the pushover maneuver. Notably, the pilot appears to decelerate more gradually in the initial stages of the flare. However, the longitudinal speed at touchdown is similar for piloted and autonomous simulations (*i.e.*, approximately 20 kts). It is also worth noting that the lateral speed for the autonomous simulation remains approximately constant throughout the flare maneuver, which indicates good off-axis disturbance rejection from the NDI control law. Figure 8b shows the longitudinal position and altitude of the helicopter. In this figure, it is shown that longitudinal position and altitude trajectories from piloted and autonomous simulations are very similar, which indicates the validity of the proposed approach. As shown in Fig. 8c, pushover is initiated by the pilot at approximately 8 seconds into flare, whereas the autonomous control law delays pushover to the ninth second. Despite this difference, pitch attitudes at touchdown are similar, *i.e.*, approximately 10 deg. In this figure it is also shown that the roll and yaw attitudes for the autonomous flare remain contained which, again, indicates good performance of the controller in mitigating the off-axis response.

Finally, Fig. 8d shows the time histories for the main rotor angular speed and collective angle. These variables follow the trend of typical flare maneuvers, where the main rotor angular speed first increases due increase in inflow due to the pitch up, and then decreases significantly as the rotor trades kinetic energy to decelerate the vehicle. Similarly, the main rotor collective angle increases gradually at the beginning of the flare to reduce the vertical speed, and increases more rapidly during the pushover. These results suggest that a control law based on linearized models obtained in steady-state autorotation, in conjunction with a trajectory generation algorithm based on optical Tau theory, is suitable for performing autonomous flare maneuvers in helicopter autorotation. More specifically, trajectories generated with optical Tau theory are shown to be similar to those employed by pilots in flare maneuvers, whereas the NDI control law is shown to accurately track these trajectories in this example case.

B. Reachability Study

Because the NDI controller is capable of performing autonomous autorotative flare maneuvers, it can be used as a tool for determining which combinations of downrange distances and altitudes at flare entry result in a successful landing. Touchdown performance is measured by comparing critical rotorcraft state touchdown parameters against guideline metrics for desired and adequate touchdown in Ref. 30 and reported in Table 8. This table also includes bounds on the angular speed of the main rotor, which is not only evaluated at touchdown but throughout the flare maneuver. Minimum rotor speed is evaluated only until pushover.

Table 8 Conditions for successful and marginal autorotative landings.

	V_x [ft/s]	V_z [ft/s]	θ [deg]	q [deg/s]	Ω/Ω_0 [%]
Desired	< 30	< -8	< 12	-30 to 20	90 to 110
Marginal	< 60	< -15	< 20	-50 to 40	80 to 120

As such, a parametric study is conducted in which flare maneuvers are simulated for varying downrange distances of the intended landing point and altitudes at flare entry. Downrange distances vary from 800 to 1,200 ft from the flare initiation point in increments of 20 ft, whereas altitudes at flare entry vary between 100 and 200 ft in increments of 10 ft. These ranges were chosen based on indications from previous studies (*e.g.*, Ref. 31) involving piloted simulations, and on the piloted simulation data described above. Flare maneuvers are initiated at 80 kts total speed and at an aircraft weight of 16,270 lb so as to be consistent with the parameters used in the piloted simulations. Figure 9 shows the critical aircraft state parameters for those flare maneuvers simulated as part of this parametric study. Figure 9a shows that the longitudinal speed at touchdown tends to be higher for high downrange distances and low altitudes at flare entry. This is because, as shown in Fig. 1a, the deceleration in longitudinal speed for high downrange distances is concentrated at the end of the trajectory. As such, the helicopter has limited time and altitude to slow down before it pitches over upon touchdown. The premature pitch-over causes the longitudinal speed to stop decreasing ahead of time and thus remains relatively high. Figure 9b shows that the vertical speed at touchdown is within the adequate bounds for most of the downrange distances and altitude considered, except for low altitudes and downrange distances at flare entry. Figure 9c shows that low altitudes at flare entry generally result in low pitch attitudes at touch down. On the other hand, low

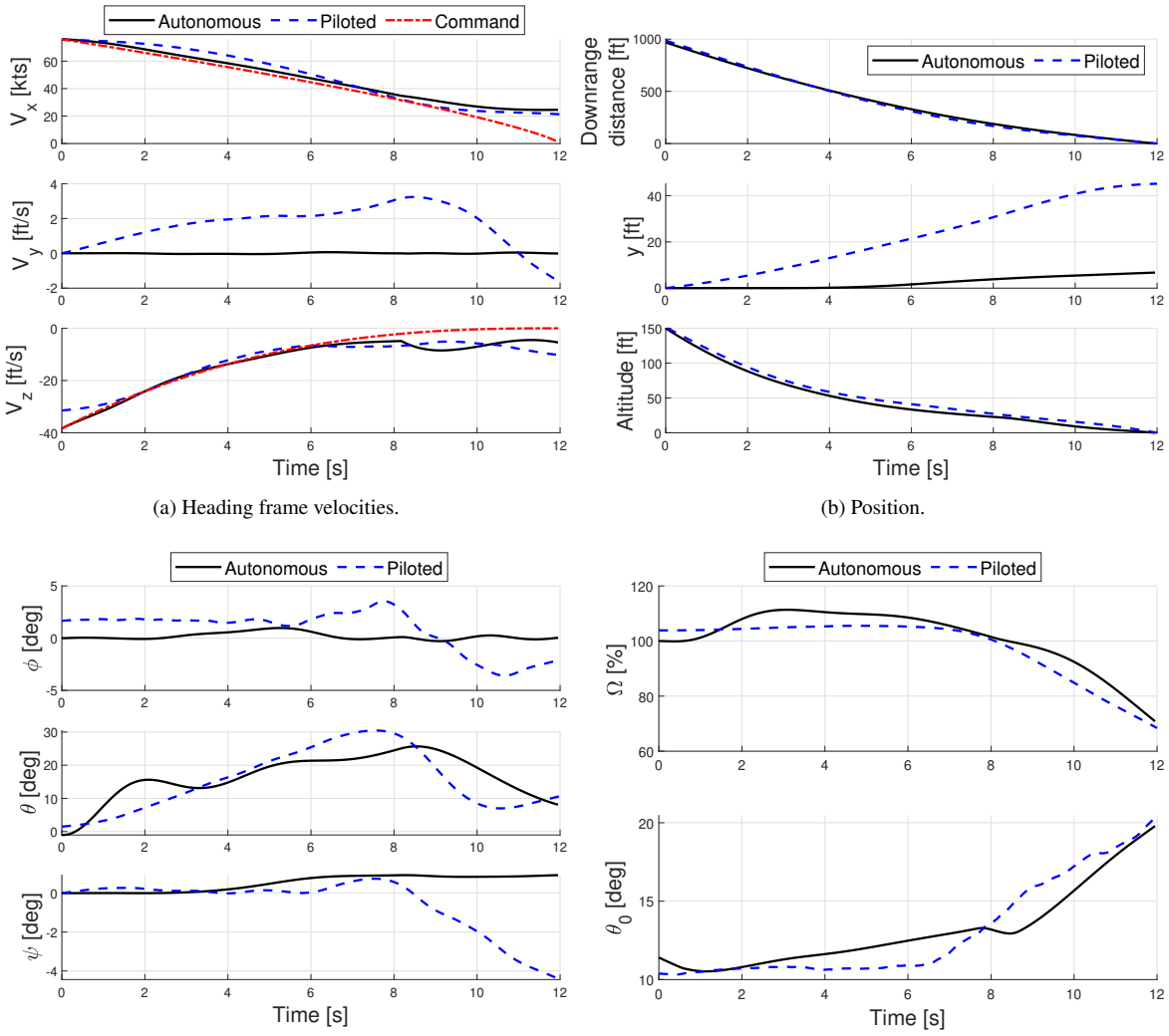

(a) Heading frame velocities.

(b) Position.

(c) Euler angles.

(d) Longitudinal cyclic, collective, and main rotor speed.

Fig. 8 Example of flare trajectories generated with optical Tau theory and tracked by the helicopter augmented with a nonlinear dynamic inversion control law.

downrange distances and high altitudes result in higher pitch angles at touch down. Figure 9d shows that pitch rate at touchdown is largely within the desired boundaries. Figure 9e shows that minimum rotor speed requirements are met for all conditions. On the other hand, maximum desired rotor speed limits are exceeded for low downrange distances and high flare initiation altitudes, as shown in Fig. 9f.

Based on the results from the parametric study, combinations of downrange distances and altitudes at flare initiation that give successful and marginal landings are shown in Fig. 10. In this figure, conditions for successful touchdown are marked in black, whereas those for marginal touchdown are marked in gray. Successful autorotation for the flight condition in consideration (*i.e.*, 80 kts total speed and aircraft weight of 16,270 lb) is achieved for moderate to high downrange distances (*i.e.*, 920 to 1,150 ft) and moderate altitudes at flare initiation (*i.e.*, 130 to 180 ft). Successful and marginal piloted autorotations, still evaluated with the criteria in Table 8, are overlaid on the reachability plot obtained from autonomous flares. Although two desired piloted autorotations were performed for conditions that gave marginal landings in autonomous simulations, most desired and marginal autorotations fall within those desired and marginal bounds predicted using the autonomous control law.

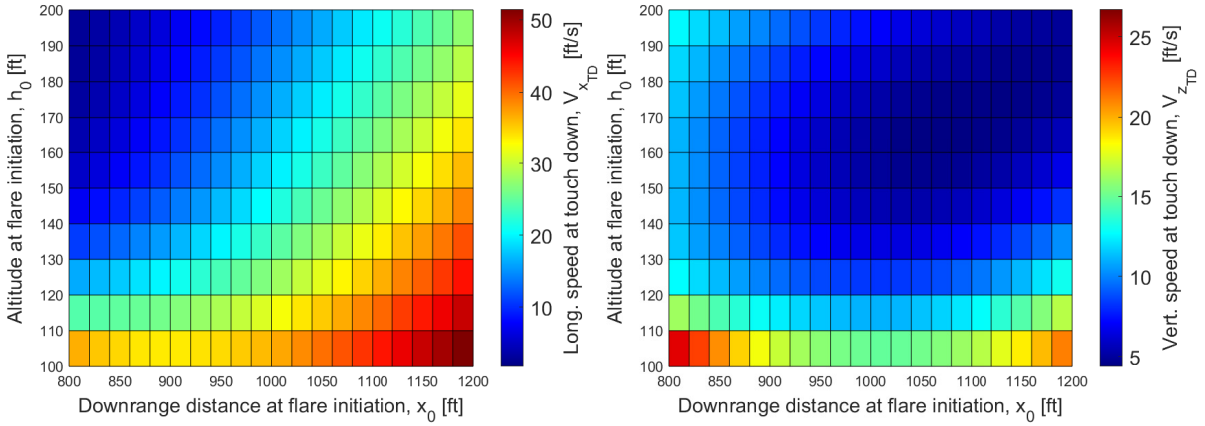

(a) Longitudinal speed at touchdown.

(b) Vertical speed at touchdown.

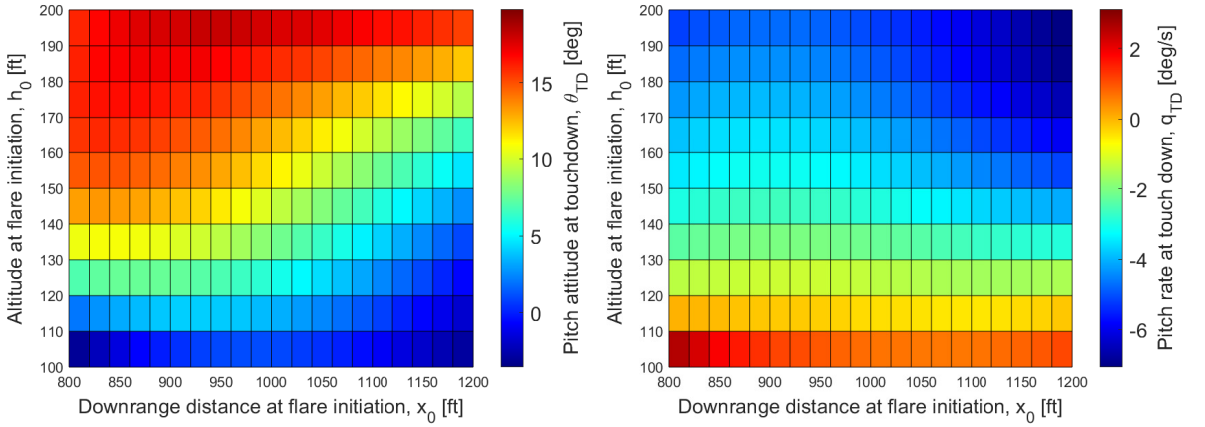

(c) Pitch attitude at touchdown.

(d) Pitch rate at touchdown.

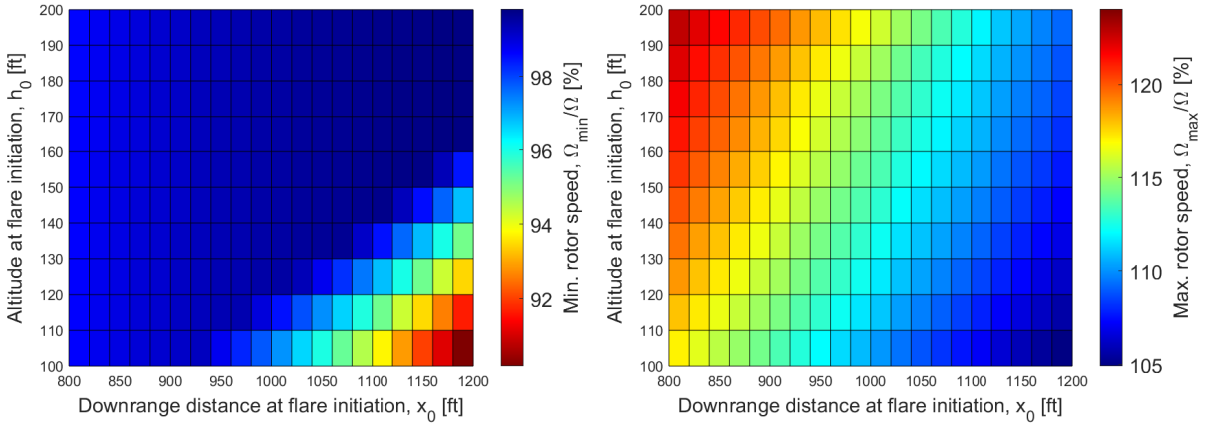

(e) Mininum rotor speed.

(f) Maximum rotor speed.

Fig. 9 Critical aircraft state parameters for flare maneuvers initiated at varying downrange distances and altitudes.

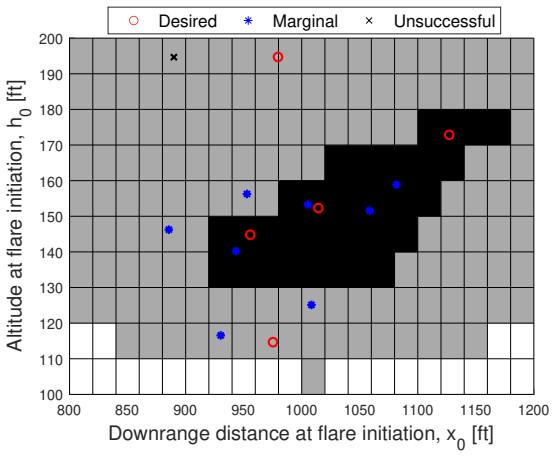

Fig. 10 Combination of downrange distances and altitudes at flare entry for successful (black markers) and marginal (gray markers) autonomous landings. Desired, marginal, and unsuccessful pilot landings are shown with red circles, blue asterisks, and black crosses, respectively.

VI. Conclusion

A novel trajectory generation and control architecture for fully autonomous autorotation flare was proposed that combines rapid path generation with model-based control. The trajectory generation component uses optical Tau theory to rapidly compute flare trajectories for both longitudinal and vertical speed. These flare trajectories are tracked by a nonlinear dynamic inversion (NDI) control law scheduled with linear systems obtained in steady-state autorotation at varying speeds. Computer simulations were used to demonstrate that the NDI control law is able to successfully execute autorotative flare in the UH-60 aircraft. Simulations of the autonomous flare algorithm are compared with piloted simulation data to assess the similarities and/or discrepancies between the autonomous flare strategies and those used by real pilot. Trade studies examine the combinations of downrange distances and altitudes at flare initiation that result in successful and marginal autorotative landings. Based on this work, the following conclusions can be reached.

1) Scheduling of the NDI control law with linearized models of the rotorcraft flight dynamics in steady-state autorotation was shown to be a successful approach for tracking flare trajectories. In addition to achieving adequate tracking of the longitudinal and vertical trajectories, the control law also shows good performance in mitigating the off-axis response.
2) State histories of the autonomous flare maneuvers largely mimic those of piloted flight simulations. Noticeable differences lie in a more aggressive longitudinal deceleration in the early stages of flare, and a delayed pitchover before landing.
3) The proposed method was used to predict combinations of downrange distances and altitudes at flare entry that result in desired and marginal landings. These predictions are in line with piloted flight simulation data, suggesting that the method can be used not only for real-time control but also for reachability predictions in autorotation flare.

Acknowledgments

This research was partially funded by the Government under Agreements No. W911W6-17-2-0002 and No. W911NF-16-2-0027. The U.S. Government is authorized to reproduce and distribute reprints for Government purposes notwithstanding any copyright notation thereon. The U.S. Government technical monitor is Mahendra Bhagwat. The views and conclusions contained in this document are those of the authors and should not be interpreted as representing the official policies, either expressed or implied, of the Aviation Development Directorate or the U.S. Government.

References

[1] Bachelder, E. N., and Aponso, B. L., "Using Optimal Control for Rotorcraft AutorotationTraining," *Proceedings of the 59th Annual Forum of the American Helicopter Society*, AHS, Phoenix, AZ, May 6-8, 2003.

[2] Aponso, B. L., Lee, D., and Bachelder, E. N., "Evaluation of a Rotorcraft Autorotation Training Display on a Commercial Flight Training Device," *Journal of the American Helicopter Society*, Vol. 52, No. 2, 2007, pp. 123–133. https://doi.org/10.4050/JAHS.52.123.

[3] Keller, J. D., McKillip, R., Horn, J. F., and Yomchinda, T., "Active Flight Control and Appliqué Inceptor Concepts for Autorotation Performance Enhancement," *Proceedings of the 67th Annual Forum of the American Helicopter Society*, AHS, Virginia Beach, VA, May 3-5, 2011.

[4] Sunberg, Z. N., Miller, N. R., and Rogers, J. D., "A Real-Time Expert Control System For Helicopter Autorotation," *Journal of the American Helicopter Society*, Vol. 60, No. 2, 2015, pp. 1–15(15). https://doi.org/10.4050/JAHS.60.022008.

[5] Rogers, J., Repola, L., Jump, M., Cameron, N., and Fell, T., "Handling Qualities Assessment of a Pilot Cueing System for Autorotation Maneuvers," *Proceedings of the 73rd Annual Forum of the American Helicopter Society*, AHS, Ft. Worth, TX, May 9-11, 2017.

[6] Yomchinda, T., "REAL-TIME PATH PLANNING AND AUTONOMOUS CONTROL FOR HELICOPTER AUTOROTATION," Ph.D. thesis, Pennsylvania State University, May, 2013.

[7] Yomchinda, T., Horn, J., and Langelaan, J., "Flight Path Planning for Descent-phase Helicopter Autorotation," *AIAA Guidance, Navigation and Control Conference*, AIAA, Portland, OR, Aug 8-11, 2011.

[8] Grande, N., Tierney, S., Horn, J., and Langelaan, J., "Safe Autorotation Through Wind Shear Via Backward Reachable Sets," *Journal of the American Helicopter Society*, Vol. 61, No. 2, 2016, pp. 1–11. https://doi.org/10.4050/JAHS.61.022006.

[9] Tierney, S., and Langelaan, J., "Autorotation path planning using backwards reachable set and optimal control," *Annual Forum Proceedings - AHS International*, Vol. 3, 2010, pp. 1895–1907. 66th Forum of the American Helicopter Society: "Rising to New Heights in Vertical Lift Technology", AHS Forum 66 ; Conference date: 11-05-2010 Through 13-05-2010.

[10] Eberle, B. F., and Rogers, J. D., "Real-Time Trajectory Generation and Reachability Determination in Autorotative Flare," *Journal of the American Helicopter Society*, Vol. 65, No. 3, 2020, pp. 1–17(17). https://doi.org/10.4050/JAHS.65.032008.

[11] Horn, J. F., "Non-Linear Dynamic Inversion Control Design for Rotorcraft," *Aerospace*, Vol. 6, No. 3, 2019. https://doi.org/10.3390/aerospace6030038.

[12] Saetti, U., Horn, J. F., Villafana, W., Sharma, K., and Brentner, K. S., "Rotorcraft Simulations with Coupled Flight Dynamics, Free Wake, and Acoustics," *Proceedings of the 72nd Annual Forum of the American Helicopter Society*, 2016.

[13] Saetti, U., Horn, J. F., Lakhmani, S., Lagoa, C., and Berger, T., "Design of Dynamic Inversion and Explicit Model Following Control Laws for Quadrotor UAS," *Journal of the American Helicopter Society*, Vol. 65, No. 3, 2020, pp. 1–16(16). https://doi.org/10.4050/JAHS.65.032006.

[14] Caudle, D. B., "DAMAGE MITIGATION FOR ROTORCRAFT THROUGH LOAD ALLEVIATING CONTROL," Master's thesis, The Pennsylvania State University, 2014.

[15] Spires, J. M., and Horn, J. F., "Multi-Input Multi-Output Model-Following Control Design Methods for Rotorcraft," *Proceedings of the 71st Annual Forum of the American Helicopter Society*, 2015.

[16] Saetti, U., Enciu, J., and Horn, J. F., "Flight Dynamics and Control of an eVTOL Concept Aircraft with a Propeller-Driven Rotor," *Proceedings of the 76nd Annual Forum of the Vertical Flight Society*, 2020.

[17] Padfield, G. D., *Helicopter Flight Dynamics: Including a Treatment of Tiltrotor Aircraft*, John Wiley & Sons, 2018.

[18] Pitt, D. M., and Peters, D. A., "Theoretical Prediction of Dynamic-Inflow Derivatives," *Vertica*, Vol. 5, No. 1, 1883, pp. 21–34.

[19] Leishman, J. G., *Principles of Helicopter Aerodynamics*, Cambridge University Press, 2006.

[20] Lee, D., "A Theory of Visual Control of Braking Based on Information about Time-to-Collision," *Perception*, Vol. 5, 1976, pp. 437–459.

[21] Alam, M., Jump, M., Eberle, B., and Rogers, J., "Flight Simulation Assessment of Autorotation Algorithms and Cues," *Proceedings of the 76th Annual Forum of the Vertical Flight Society*, 2020.

[22] Howlett, J. J., "UH-60A Black Hawk Engineering Simulation Program. Volume 1: Mathematical Model," Tech. rep., NASA-CR-166309, 1980.

[23] Blakelock, J. H., *Automatic Control of Aircraft and Missiles*, John Wiley & Sons, 1965. https://doi.org/10.1017/S0001924000057912.

[24] Stevens, B. L., and Lewis, F. L., *Aircraft Control and Simulation: Dynamics, Controls Design, and Autonomous Systems, Third Edition*, John Wiley and Sons, Inc., 2015.

[25] Tischler, M. B., Berger, T., Ivler, C. M., Mansur, M. H., Cheung, K. K., and Soong, J. Y., *Practical Methods for Aircraft and Rotorcraft Flight Control Design: An Optimization-Based Approach*, American Institute of Aeronautics and Astronautics, Reston, VA, 2017.

[26] White, M. D., Perfect, P., Padfield, G. D., Gubbles, A. W., and Berryman, A. C., "Acceptance Testing and Conditioning of a Flight Simulator for Rotorcraft Simulation Fidelity Research," *Proceedings of the Institution of Mechanical Engineers Part G Journal of Aerospace Engineering*, Vol. 227, No. 4, 2013, pp. 663–686. https://doi.org/10.1177/0954410012439816.

[27] Cameron, N., White, D., Mark, Perfect, P., Jump, M., and Padfield, G. D., "University of Liverpool Networked Simulations Case Studies into Recreating the Past and Shaping the Future," *2nd HELI World Conference*, Main, Germany, Nov 3-4, 2010.

[28] Alam, M., Jump, M., and Cameron, M., "Can Time-To-Contact Be Used To Model A Helicopter Autorotation?" *Proceedings of the 8th Asian/Australian Rotorcraft Forum*, 2019.

[29] Jump, M., Alam, M., Rogers, J. D., and Eberle, B., "Progress in the Development of a Time-To-Contact Autorotation Cueing System," *Proceedings of the 44th European Rotorcraft Forum*, 2018.

[30] Padfield, G. D., "The Tau of Flight Control," *The Aeronautical Journal*, Vol. 115, No. 1171, 2011, pp. 521–556.

[31] Rogers, J. D., Eberle, B. F., Jump, M., and Cameron, N., "Time-to-Contact-Based Control Laws for Flare Trajectory Generation and Landing Point Tracking in Autorotation," *Proceedings of the 74th Annual Forum of the Vertical Flight Society*, 2018.